

## Load assessment of optimally-arranged point absorbers arrays in front of a vertical wall

Loukogeorgaki, Eva; Michailides, Constantine ; Lavidas, G.; Saeidtehrani, S.; Chatjigeorgiou, Ioannis K.

**DOI**

[10.1201/9781003360773-27](https://doi.org/10.1201/9781003360773-27)

**Publication date**

2022

**Document Version**

Final published version

**Published in**

Trends in Renewable Energies Offshore - Proceedings of the 5th International Conference on Renewable Energies Offshore, RENEW 2022

**Citation (APA)**

Loukogeorgaki, E., Michailides, C., Lavidas, G., Saeidtehrani, S., & Chatjigeorgiou, I. K. (2022). Load assessment of optimally-arranged point absorbers arrays in front of a vertical wall. In C. Guedes Soares (Ed.), *Trends in Renewable Energies Offshore - Proceedings of the 5th International Conference on Renewable Energies Offshore, RENEW 2022* (pp. 231-240). (Trends in Renewable Energies Offshore - Proceedings of the 5th International Conference on Renewable Energies Offshore, RENEW 2022). CRC Press. <https://doi.org/10.1201/9781003360773-27>

**Important note**

To cite this publication, please use the final published version (if applicable). Please check the document version above.

**Copyright**

Other than for strictly personal use, it is not permitted to download, forward or distribute the text or part of it, without the consent of the author(s) and/or copyright holder(s), unless the work is under an open content license such as Creative Commons.

**Takedown policy**

Please contact us and provide details if you believe this document breaches copyrights. We will remove access to the work immediately and investigate your claim.

***Green Open Access added to TU Delft Institutional Repository***

***'You share, we take care!' - Taverne project***

**<https://www.openaccess.nl/en/you-share-we-take-care>**

Otherwise as indicated in the copyright section: the publisher is the copyright holder of this work and the author uses the Dutch legislation to make this work public.

# Load assessment of optimally-arranged point absorbers arrays in front of a vertical wall

E. Loukogeorgaki

*Civil Engineering Department, Aristotle University of Thessaloniki, Thessaloniki, Greece*

C. Michailides

*Civil Engineering Department, International Hellenic University, Serres, Greece*

G. Lavidas & S. Saeidtehrani

*Civil Engineering and Geosciences Department, Delft University of Technology, Delft, The Netherlands*

I.K. Chatjigeorgiou

*Naval Architecture and Marine Engineering School, National Technical University of Athens, Athens, Greece*

**ABSTRACT:** In this paper, we assess numerically the loads applied on PAs of optimally-arranged linear arrays in front of a bottom-mounted vertical wall of finite length under normal operating conditions. The arrays, maximizing the yearly absorbed energy, consist of five, identical, oblate spheroidal heaving PAs and are deployed at three near-shore sites in the Aegean Sea, Greece. The PAs are assumed to be attached on the wall via connection configurations restraining all rigid-body modes except heave. A spectral analysis is performed to quantify loads. The corresponding transfer functions are obtained from a frequency-based hydrodynamic model that solves the diffraction/radiation problem of the multi-body arrangement in the presence of the wall. Results, focusing on surge and sway restraining loads, are, initially, presented for regular waves and, then, for normal operating conditions (irregular waves), highlighting the effect of the arrays' layouts and of the local wave conditions on the restraining loads. Comparison is also made with equally-spaced arrays to reveal potential positive effects of optimum layouts on structural integrity related issues.

## 1 INTRODUCTION

The sustainable development and utilization of different types of offshore renewable energy technologies are desired to reach the 2030 climate objectives and achieve carbon neutrality by 2050 as set by EU (European Commission 2019). The efficient exploitation of the vast available wave energy resource could contribute to the above, offering at the same time multiple benefits to coastal countries and communities.

Within the above context, the Wave Energy Converters (WECs) technology is picking up speed during the last years. Various WECs have been designed and tested so far (e.g. Ahamed et al. 2020, Portillo et al. 2020), with the Point Absorbers (PAs) representing, nowadays, one of the two most advanced and technologically mature device types (Magagna et al. 2016). At the same time, design methods, tools and criteria to tackle efficiency and structural integrity related issues are in a reconsideration phase, while different development paths have been raised, including among others: (a) scaling up of the devices' power absorption ability offshore or nearshore by deploying multi-body

arrays (e.g. Penalba et al. 2017, Giassi & Götteman 2018) and (b) integration of WECs technologies (isolated devices or WEC arrays) with coastal structures at nearshore locations (e.g. Michailides & Angelides 2015, Zhao et al. 2019), supporting cost-efficient solutions through costs sharing.

Most WECs are designed in order to operate in their resonance limits and in a big number of cyclic dynamic loading. Therefore, optimum solutions in terms of both power efficiency and structural integrity should be targeted, not only on the device level, but also on the array level. Accordingly, different optimization methods and tools have been developed and applied to solve single- or multi- objective optimization problems for WECs shape optimization (e.g. Garcia-Teruel & Forehand 2021, Guo & Ringwood 2021) and for WEC array layout optimization (e.g. Fang et al. 2018, Lyu et al. 2019) including various design variables and thresholds. Traditional evolutionary optimization algorithms (e.g. Ruiz et al. 2017, Sharp & DuPont 2018) or other advanced approaches, such as the machine learning approach (e.g. Sarkar et al. 2016) and the artificial neural

networks (e.g. Neshat et al. 2019) have been used for the layout optimization of WEC arrays. On the other hand, within the context of integrating WECs with coastal structures, Loukogeorgaki et al (2021a, b) determined the optimum layout of arrays of heaving PAs in front of a vertical, bottom-mounted wall of finite length at different near-shore sites of mild wave environments in the Aegean Sea, Greece. In all the above studies, emphasis is mainly given on the produced power and the efficiency of the WEC array as well as on cost related issues, dominated mostly by the produced power factor. It is, however, questionable what the effects of the optimum array configurations on structural integrity related issues are.

Motivated by this, the present paper focuses on the load assessment of optimally-arranged linear arrays of heaving PAs in front of a vertical, bottom-mounted wall under normal operating conditions. Optimum layouts maximize the yearly energy absorbed by the array at a given marine site and satisfy predefined spatial constraints. Each PA is assumed to be attached on the wall via a connection configuration that restrains all rigid-body modes except the one corresponding to heave. Loads quantification is realized by the means of a spectral analysis. The transfer functions (unit-amplitude loads) required for this analysis are obtained from a linear frequency-based hydrodynamic model, which solves the complete diffraction and radiation problem of the multi-body arrangement in the presence of the wall. Load assessment is implemented for optimally-arranged arrays that consist of five, identical, oblate spheroidal heaving PAs (Loukogeorgaki et al. 2021a) and are deployed at three near-shore sites in the Aegean Sea, Greece, characterized by different wave climates. The required sea states characterization is acquired by a numerical wave model, specifically developed for the Aegean Sea. Results, focusing on the surge and sway restraining loads, are initially presented for regular waves to highlight critical features of the loading transfer functions. Next, the results for normal operating conditions (irregular waves) are cited and discussed, with an emphasis on the effect of the arrays' layouts and of the local wave conditions on the examined restraining loads. Comparisons with equally-spaced, non-optimized arrays are also made to reveal potential positive effects of optimum layouts on integrity-related issues.

## 2 NUMERICAL MODELLING

A linear array of  $Q$  hydrodynamically interacting semi-immersed heaving PAs is placed at a marine site of water depth  $h$  in front of bottom-mounted, vertical wall of finite length  $l_{wall}$  (Figure 1). The array consists of identical PAs that have an oblate spheroidal shape of semi-major and semi-minor axes  $a$  and  $b$  respectively (Figure 1b), and are enabled to oscillate only along the vertical

direction. The latter condition can be realized by attaching the PAs on the wall via arms, which move vertically along sliding guideways (sliders), as proposed by Gkaraklova et al. (2021) for the case a hybrid wind-wave monopile support structure. The devices are located at a distance  $c$  in front of the wall and they can be arbitrary distributed within the linear array, with the  $X$  coordinate of the center of the  $q$ -th PA,  $X_q$ ,  $q=1, \dots, Q$ , denoting the position of the device along the global  $OX$  axis. Each  $PA_q$ ,  $q=1, \dots, Q$ , is assumed to absorb power through a linear PTO mechanism, which is actuated by the device's heave forced motion and is schematically shown in Figure 1b as a linear damping system of damping coefficient  $b_{PTOq}$ .

The hydrodynamic analysis of the examined arrangement under the action of regular unit-amplitude incident waves of circular frequency  $\omega$ , considering the hydrodynamic interactions among the PAs and between the wall and the devices, is conducted in the frequency domain. It is based on the Boundary Integral Equation Method (BIEM), which is numerically realized using WAMIT© software (Lee 1995). The applied methodology relies on the three-dimensional linear potential theory, where the wall is considered fixed at its position and each PA is taken to oscillate freely only along its working direction, i.e. along the local  $oz$  axis (Figure 1b). Hence, the rigid-body modes of the PAs except the one corresponding to heave, are considered restrained (fixed). In order though to calculate the corresponding restraining loads, the complete diffraction and radiation problem has to be solved.

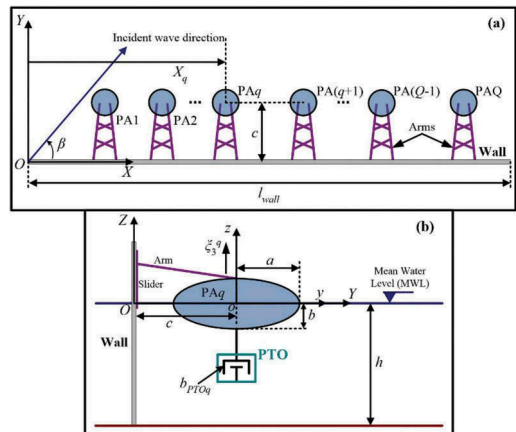


Figure 1. Geometry of the examined problem and definition of basic quantities: (a)  $X$ - $Y$  plane, (b)  $Y$ - $Z$  plane.

Assuming inviscid and incompressible fluid with irrotational flow, the fluid motion is described in terms of the velocity potential, which satisfies the Laplace equation. Its complex spatial part is defined as (Lee 1995, Lee & Newman 2005):

$$\varphi = \underbrace{\varphi_I + \varphi_S}_{\varphi_D} + i\omega \sum_{j=1}^6 \sum_{q=1}^Q \xi_j^q \varphi_j^q \quad (1)$$

$$\varphi_I = \frac{igA \cosh[k(Z+h)]}{\omega \cosh(kh)} e^{-ik(X \cos \beta + Y \sin \beta)} \quad (2)$$

where  $\varphi_I$ ,  $\varphi_S$ ,  $\varphi_D$  and  $\varphi_j^q$ ,  $j=1, \dots, 6$ ,  $q=1, \dots, Q$ , are respectively, the incident, scattered, diffracted and unit-amplitude radiation (in the  $j$ -th mode of the  $q$ -th body) potentials,  $\xi_j^q$ ,  $j=1, \dots, 6$ ,  $q=1, \dots, Q$ , are the complex amplitudes of the  $q$ -th PA surge ( $j=1$ ), sway ( $j=2$ ), heave ( $j=3$ ), roll ( $j=4$ ), pitch ( $j=5$ ) and yaw ( $j=6$ ) motions,  $A$  is the amplitude of the incident waves,  $\beta$  is the propagation angle of the waves relatively to the  $OX$  axis (Figure 1a),  $g$  is the gravitational acceleration,  $k$  is the wave number and  $i^2=-1$ .

The first order boundary value problem is formed by subjecting the potentials to the combined kinematic and dynamic free-surface boundary condition, the bottom boundary condition and the Neumann boundary conditions on the wetted surface of the bodies (Lee 1995, Lee & Newman 2005). Then, the boundary integral equations for the unknown diffraction and radiation potentials on the boundary of the PAs and the wall, and of the PAs respectively are formulated by deploying Green's theorem, and the boundary value problem is solved based on a three dimensional high-order panel method (Lee 1995, Lee & Newman 2005).

Subsequently, first order hydrodynamic quantities (exciting forces, hydrodynamic coefficients) are calculated as:

$$F_j^q = -i\omega\rho \iint_{S_{Bq}} n_j^q \varphi_D ds \quad (3)$$

$$A_{ij}^{ql} - \frac{i}{\omega} B_{ij}^{ql} = \rho \iint_{S_{Bq}} n_i^q \varphi_j^l ds \quad (4)$$

where  $F_j^q$ ,  $j=1, \dots, 6$ ,  $q=1, \dots, Q$ , is the exciting force of the  $j$ -th rigid-body mode of the  $q$ -th PA,  $A_{ij}^{ql}$  and  $B_{ij}^{ql}$ ,  $i, j=1, \dots, 6$ ,  $q, l=1, \dots, Q$ , are the added mass and radiation damping coefficients, respectively, in the  $i$ -th degree of freedom of the  $q$ -th PA due to the  $j$ -th mode of motion of the  $l$ -th PA,  $n_i^q$  is the  $i$ -th component of the normal vector of the  $q$ -th PA and  $\rho$  is the seawater density.

Considering the existence of restrained surge, sway and rotational rigid-body modes for all the PAs, the complex amplitudes of the devices' heave motions,  $\xi_3^l$ ,  $l=1, \dots, Q$ , are obtained from the solution of the following linear system of equations:

$$\sum_{l=1}^Q \left[ \begin{array}{c} -\omega^2(m_q \delta_{ql} + A_{33}^{ql}) + \\ + i\omega(B_{33}^{ql} + b_{PTOq} \delta_{ql}) + C_{33}^q \delta_{ql} \end{array} \right] \xi_3^l = F_3^q, q = 1, \dots, Q \quad (5)$$

where,  $m_q$  and  $C_{33}^q$  are respectively the submerged mass and the heave hydrostatic stiffness coefficient of the  $q$ -th PA and  $\delta_{ql}$  is the Kronecker delta.

Following the solution of Equation 5, the restraining loads result from:

$$FR_j^q = F_j^q - \sum_{l=1}^Q \left[ \begin{array}{c} -\omega^2(M_{j3}^{ql} + A_{j3}^{ql}) + \\ + i\omega B_{j3}^{ql} + C_{j3}^{ql} \end{array} \right] \xi_3^l, \quad (6)$$

$q = 1, \dots, Q$  and  $j = 1, 2, 4, 5, 6$

where  $FR_j^q$  corresponds to the restraining load applied in the  $j$ -th degree of freedom of the  $q$ -th PA, while,  $M_{j3}^{ql}$  and  $C_{j3}^{ql}$ , are the mass and hydrostatic-gravitational stiffness coefficients, respectively, in the  $j$ -th degree of freedom of the  $q$ -th PA due to the heave motion of the  $l$ -th PA.

Having obtained  $FR_j^q$  for various values of  $\omega$  representing the frequency components of a spectrum, a spectral analysis follows to quantify the loads applied on the PAs for the local wave climate conditions (set of sea states) characterizing the marine site, where the array is deployed. Specifically, for a given sea state described by a spectrum with significant wave height,  $H_s$ , and peak period,  $T_p$ , the spectrum of the  $j$ -th restraining load for the  $q$ -th PA,  $SFR_j^q(\omega | H_s, T_p)$ , results from:

$$SFR_j^q(\omega | H_s, T_p) = \int_0^\infty |FR_j^q|^2 S(\omega | H_s, T_p) d\omega \quad (7)$$

where  $|FR_j^q|$  is the amplitude of the complex quantity  $FR_j^q$  (i.e. loading transfer function) and  $S(\omega | H_s, T_p)$  is the spectral density of the examined incident wave spectrum, with the symbol “|” denoting given values of  $H_s$  and  $T_p$ .

Based on the loads spectra, the restraining load applied in the  $j$ -th degree of freedom of the  $q$ -th PA for a given  $H_s$  and  $T_p$  combination is then expressed in terms of the Root Mean Square (RMS) value,  $FR_j^{qRMS}(H_s, T_p)$ , using Equation 8 (e.g. Naess & Moan 2013):

$$FR_j^{qRMS}(H_s, T_p) = \sqrt{SFR_j^q(\omega | H_s, T_p)} \quad (8)$$

Additionally to the above, the annual averaged energy,  $E_{annual}$ , absorbed by the array under operating conditions for a given marine site can be estimated as follows (Loukogeorgaki et al. 2021a):

$$E_{annual} = 8,760 \left( \sum_{H_s} \sum_{T_p} Pr(H_s, T_p) p(H_s, T_p) \right) \quad (9)$$

where  $P_s(H_s, T_p)$  is the annual probability of occurrence of a sea state and  $p(H_s, T_p)$  is the power absorbed by the array for the specific sea state resulting from:

$$p(H_s, T_p) = \sum_{q=1}^Q \int_0^{\infty} S(\omega|H_s, T_p) p_q(\omega) d\omega \quad (10)$$

In Equation 10,  $p_q(\omega)$  is the average power absorbed by the  $q$ -th PA of the array for a unit-amplitude regular wave of frequency  $\omega$ , calculated as follows:

$$p_q(\omega) = 0.5 b_{PTOq} \omega^2 |\zeta_3^q|^2 \quad (11)$$

where  $|\zeta_3^q|$  denotes the amplitude of the complex quantity  $\zeta_3^q$ .

### 3 EXAMINED CASES

A linear array of  $Q=5$  oblate spheroidal PAs (Figure 1a with  $Q=5$ ) in the seaward side of a wall of total non-dimensional length  $l_{wall}/a=36$  and of negligible thickness is examined. Each  $q$ -th PA has semi-major axis  $a=2.0$  m, non-dimensional semi-minor axis  $b/a=0.85$  and a constant damping coefficient  $b_{PTOq}=10.322$  kN/m (Loukogeorgaki et al. 2021a). The latter coefficient has been taken equal to  $B_{33}(\omega=\omega_{n3})$ , where  $B_{33}$  is the heave radiation damping of a single, isolated PA at its heave natural frequency,  $\omega_{n3}$  (equal to 2.4 rad/s). The whole arrangement is utilized at three different marine sites corresponding to near-shore locations at Siros (Site S1), Anafi (Site S2) and Kasos (Site S3) islands in the Aegean Sea, Greece (Figure 2).



Figure 2. Location of examined marine sites in the Aegean Sea, Greece.

Load assessment is implemented for optimally-arranged arrays that maximize  $E_{annual}$  at each examined marine site, while satisfying specific spatial constraints. The optimum layouts of these arrays have been determined by Loukogeorgaki et al. (2021a) and are shown schematically in Figure 3. It can be seen that for all three sites the optimally-arranged arrays are placed at a non-dimensional distance from the wall  $c/a$  equal to 1.1 and are characterized by the formation of two clusters of closely-positioned PAs. Aiming to reveal potential positive effects of optimum layouts on structural integrity related issues, results are also compared with those of equally-spaced, non-optimized arrays. In this case, all the devices are located at  $c/a=1.1$  in front of the wall and they are distributed along the whole wall length with a non-dimensional center-to-center distance equal to  $8.5a$  (Figure 4).

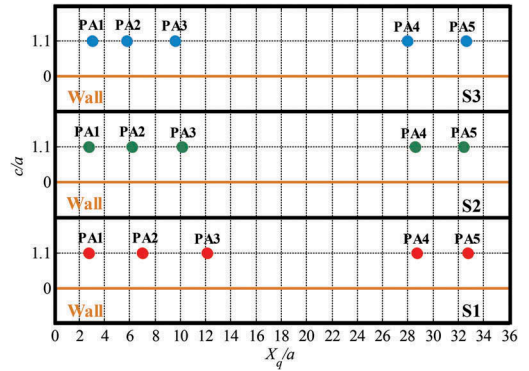


Figure 3. Examined optimum layouts of the PA array in front of the wall for sites S1-S3.

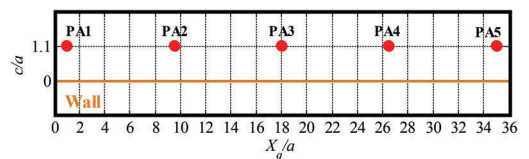


Figure 4. Layout of equally-spaced arrays in front of the wall for all examined sites.

The hydrodynamic analysis is conducted for non-dimensional water depth  $h/a$  equal to 3.5, 4 and 5 for S1, S2 and S3 respectively under the action of regular, unit-amplitude perpendicular to the wall (i.e.  $\beta=270$  deg, Figure 1a) waves with  $\omega$  varying between 0.05 rad/s and 4.0 rad/s. These values have been also considered as the cut-off spectral frequencies in the spectral analysis (e.g. Equation 7), which, has been conducted in the present investigation by utilizing the TMA spectrum (e.g. Hughes 1984, Bergdahl 2009). This spectrum corresponds

to a modified Jonswap spectrum in shallow waters and it enables the consideration of limited water depth conditions through a finite depth spectral formulation. Specifically, for a sea state with  $H_s$  and  $T_p$ ,  $S(\omega | H_s, T_p)$  for the TMA spectrum is obtained by multiplying the spectral density of the Jonswap spectrum (DNV-GL 2017) with the so-called “limited depth” function,  $\Phi(h, \omega)$ , obtained as (Bergdahl 2009):

$$\Phi(h, \omega) = \begin{cases} 0.5 \left( \omega \sqrt{h/g} \right)^2 & \omega \sqrt{h/g} < 1 \\ 1.0 - 0.5 \left( 2 - \omega \sqrt{h/g} \right)^2 & 1 \leq \omega \sqrt{h/g} < 2 \\ 1.0 & \omega \sqrt{h/g} \geq 2 \end{cases} \quad (12)$$

Regarding sea states characterization, the present work focuses on normal operating conditions. Accordingly, the corresponding wave climate matrices for all three examined marine sites have been obtained by a 35-years (1980 to 2014) hind-cast, based on the spectral phased averaged model Simulating Waves Nearshore (SWAN), specifically developed for the Aegean Sea (Lavidas & Venugopal 2017). The model utilized a two way nesting for the Mediterranean and the Aegean Seas and provided a comprehensive resource assessment, after being appropriately calibrated. Non-linear wave interactions have been taken into account within the application of SWAN for all examined marine locations.

## 4 RESULTS AND DISCUSSION

In the following sections, the results of the present investigation are presented with a focus on the surge and sway restraining loads representing the most critical ones applied on the PAs. Initially, restraining loads under the action of regular waves are discussed in order to highlight critical features of the corresponding linear transfer functions (i.e.  $FR_1^q$  and  $FR_2^q$ ,  $q=1, \dots, 5$ ) that are deployed in the subsequent spectral analysis. Next, restraining loads are presented for normal operating conditions (irregular waves), taking into account the local wave climate at each of the three examined marine sites.

### 4.1 Restraining loads under regular waves

Figures 5 and 6 show respectively the surge,  $FR_1^q$  and sway,  $FR_2^q$ ,  $q=1, \dots, 5$ , restraining loads applied on the PAs of the optimally-arranged arrays at the three examined sites. Both loads are given normalized by  $\rho g A a^2$ .

Starting with the surge restraining loads (Figure 5), non-zero values of  $FR_1^q$ ,  $q=1, \dots, 5$ , exist as a result of the hydrodynamic interactions among the PAs and between the devices and the wall. For

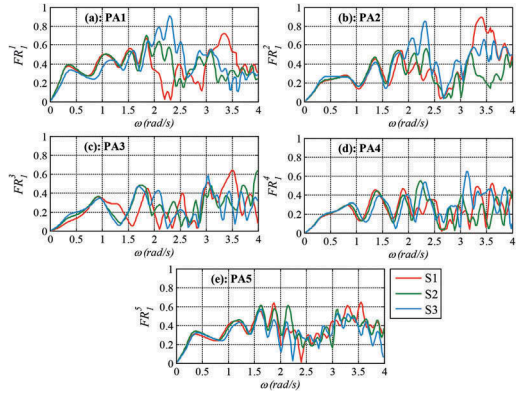


Figure 5.  $FR_1^q$ ,  $q=1, \dots, 5$ , for optimally-arranged arrays at S1-S3.

all sites examined and for all PA $q$ ,  $q=1, \dots, 5$ , an intense variation of  $FR_1^q$  as a function of  $\omega$  is observed, characterized by an irregular pattern and the existence of multiple peaks and successive local minima. The realization of different arrays’ layouts at the three examined sites introduces differences in the variation pattern and the values of  $FR_1^q$  mainly at  $\omega > 2$  rad/s, with the most significant ones observed in the case of PA1 and PA2. It is also worth to note that for a given marine site, the surge restraining loads applied on the outer PAs (i.e. PA1 and PA5) have larger values at  $\omega < 2$  rad/s compared to  $FR_1^q$ ,  $q=2, 3$  and 4.

Regarding the sway restraining loads (Figure 6), all  $FR_2^q$ ,  $q=1, \dots, 5$ , curves for a given site show a smooth variation with a peak value at  $\omega \approx 2.5$  rad/s. The location of the PAs within an optimally-arranged array lead to insignificant differences on the values of the sway restraining loads among the various devices. Similarly, the realization of different arrays’ layouts at S1-S3 affects to a quite small degree the variation pattern and the values of  $FR_2^q$ , for a specific  $q$  value.

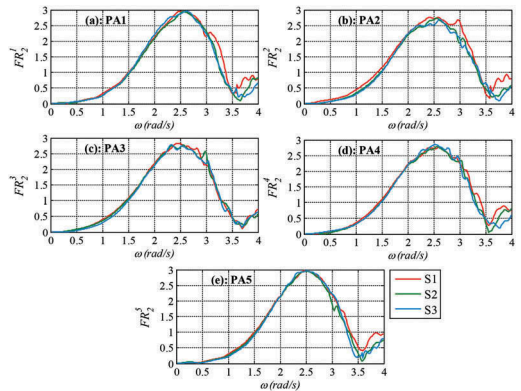


Figure 6.  $FR_2^q$ ,  $q=1, \dots, 5$ , for optimally-arranged arrays at S1-S3.

Continuing with the equally-spaced arrays, Figures 7 and 8 show respectively the corresponding surge,  $FR_1^q$  and sway,  $FR_2^q$ ,  $q=1, \dots, 5$ , restraining loads applied on the PAs at the three examined sites. It is noted that due to the symmetry of the layouts with respect to  $\beta=270$  deg,  $FR_1^3$  for the middle PA is cancelled, while  $FR_j^1=FR_j^5$  and  $FR_j^2=FR_j^4$  for  $j=1$  and 2.  $FR_1^q$ ,  $q=1, 2, 4$  and 5 (Figure 7) for all sites examined show a quite intense variation and are characterized by the existence of successive local maximum and minimum values. Furthermore, the surge exciting forces applied on the two outer PAs of the arrays (i.e. PA1 and PA5) show larger values compared to those of PA2 and PA4. On the other hand,  $FR_2^q$ ,  $q=1, \dots, 5$  (Figure 8) for all sites vary quite smoothly, with a global peak at  $\omega \approx 2.5$  rad/s, which is successively increased as we are moving from the outer devices to the middle PA (PA3). The results of Figures 7 and 8 indicate also that the consideration of different water depths at the three examined sites does not introduce any differences in the variation pattern of  $FR_1^q$  and  $FR_2^q$ , while it has a minor effect on the values of these loads.

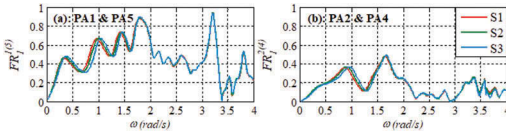


Figure 7.  $FR_1^q$ ,  $q=1, 2, 4$  and 5, for equally-spaced arrays at S1-S3.

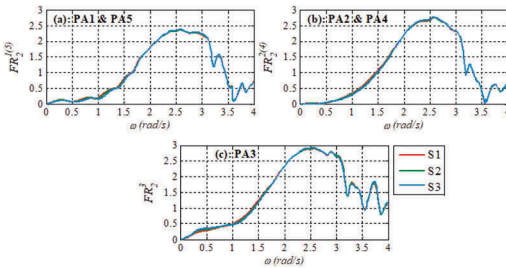


Figure 8.  $FR_2^q$ ,  $q=1, \dots, 5$ , for equally-spaced arrays at S1-S3.

Finally, by comparing the results of Figures 5-8, it can be concluded that for a given marine site, optimally-arranged arrays may lead to smaller values of the surge and sway restraining loads, depending, though, on the PA and the frequency range being examined. For example, the values of  $FR_1^q$ ,  $q=1, 2, 4$  and 5 at  $\omega < 1$  rad/s are smaller for optimally-arranged arrays (Figure 5), which, however, lead to non-zero surge restraining loads for PA3 (Figure 5c) due to the absence of symmetrical layouts with respect to the

incident wave direction. On the other hand,  $FR_2^3$  applied on PA3 has smaller values at  $\omega < 1.5$  rad/s in the case of optimally-arranged arrays (Figure 6c), while the opposite holds true when the sway restraining loads of the outer devices (PA1 and PA5) are being compared.

#### 4.2 Restraining loads for normal operating conditions

The characteristics of the local wave climate at sites S1-S3 considered for the load assessment under normal operating conditions are shown in Figure 9, where the annual probability of occurrence,  $Pr(H_s, T_p)$ , of the various sea states in percentage (%) is shown in the form of contours. For a given site, spectra and RMS values of restraining loads are calculated only for sea states that show  $Pr > 0\%$ .

For sites S1 and S2 (Figs. 9a, b) located in the Central Aegean, sea states with  $H_s, T_p$  up to 3.25 m, 11 s, and up to 4.25 m, 12 s are observed respectively, with the most frequent ones characterized by  $H_s < 1.75$  m and  $3.0 \text{ s} \leq T_p \leq 6.0$  s (site S1), and  $H_s < 2.25$  m and  $4.0 \text{ s} \leq T_p \leq 6.0$  s (site S2). As for site S3 (Figure 9c), located in South-Eastern Aegean, sea states with  $H_s$  and  $T_p$  up to 4.75 m and 13 s do exist, while large  $Pr$  values are observed for sea states with  $H_s$  up to 2.25 m and  $4.0 \text{ s} \leq T_p \leq 8.0$  s.

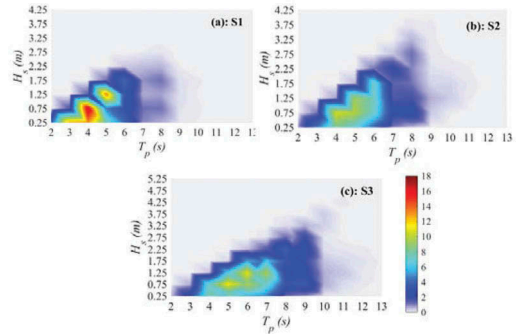


Figure 9. Local wave climate at sites S1-S3 (normal operating conditions).

It is noted that the data of Figure 9 have been also used in order to quantify  $E_{annual}$  (Equations 9-11) for the case of equally-spaced arrays. The corresponding results are included in Table 1, where also  $E_{annual}$  for optimally-arranged arrays as obtained from Louko-georgaki et al. (2021a) are cited for comparison purposes.

Table 1.  $E_{annual}$  (MWh) for optimally-arranged and equally-spaced arrays at S1-S3.

Array	S1	S2	S3
Optimally-arranged	38.124	54.093	60.822
Equally-spaced	33.353	47.785	55.854

Starting with the optimally-arranged arrays, Figures 10, 11 and 12 show the contours of  $FR_1^{qRMS}$ ,  $q=1, \dots, 5$ , at sites S1, S2 and S3 respectively.

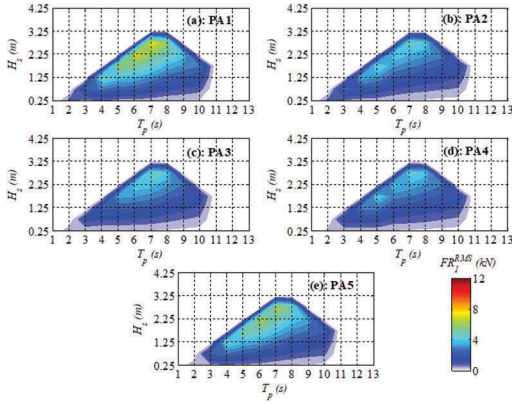


Figure 10.  $FR_1^{qRMS}$ ,  $q=1, \dots, 5$ , contours for optimally-arranged array at S1.

In the case of S1 (Figure 10),  $FR_1^{qRMS}$  peaks for all PAs are bounded at  $1.25 \text{ m} < H_s < 3.25 \text{ m}$  and  $5.0 \text{ s} \leq T_p < 8.0 \text{ s}$ . Moreover, among all the devices, the largest surge restraining loads are applied on PA1 and PA5 (outer devices), with  $FR_1^{qRMS}$ ,  $q=1$  and 5, global peaks equal to 7.6 kN and 6.7 kN respectively. This fact is related to the existence of larger values of the transfer functions  $FR_1^q$ ,  $q=1$  and 5, at  $\omega < 2 \text{ rad/s}$  (Figure 5), as previously discussed.

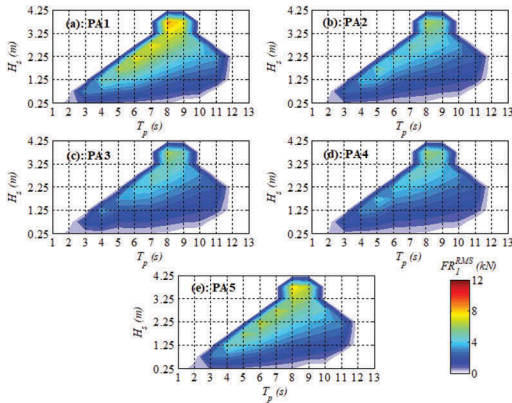


Figure 11.  $FR_1^{qRMS}$ ,  $q=1, \dots, 5$ , contours for optimally-arranged array at S2.

Regarding sites S2 and S3 (Figures 11-12), the  $FR_1^{qRMS}$  contours become wider along the  $T_p$  axis compared to S1 and they are characterized by the existence of non-zero values at  $H_s \geq 3.25 \text{ m}$ , in agreement with the local wave environments (Figures 9b, c). Accordingly,  $FR_1^{qRMS}$  peaks for all PAs are

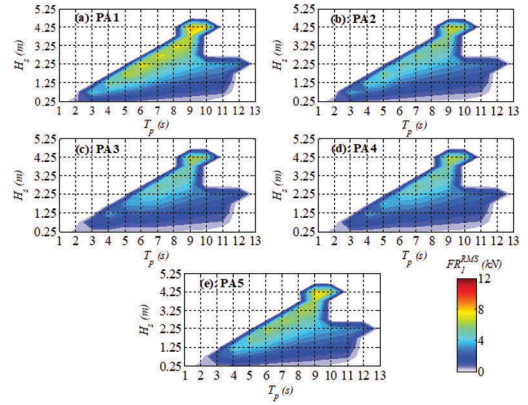


Figure 12.  $FR_1^{qRMS}$ ,  $q=1, \dots, 5$ , contours for optimally-arranged array at S3.

mainly observed at  $H_s \geq 2.25 \text{ m}$  for  $6.0 \text{ s} \leq T_p < 9.0 \text{ s}$  (site S2) and for  $6.0 \text{ s} \leq T_p < 10.0 \text{ s}$  (site S3). The consideration of different wave climate conditions for S2 and S3 leads also to a small increase of the  $FR_1^{qRMS}$  peak values for all the PAs compared to the case of S1. Still, PA1 and PA5 correspond again to the devices with the largest applied surge restraining loads, with  $FR_1^{qRMS}$ ,  $q=1$  and 5, global peaks equal respectively to: (a) 8.9 kN and 7.9 kN for S2 and (b) 8.6 kN and 7.9 kN for S3.

Continuing with the sway restraining loads, the contours of  $FR_2^{qRMS}$ ,  $q=1, \dots, 5$ , for the PAs of the optimally-arranged arrays at sites S1, S2 and S3 are shown respectively in Figures 13, 14 and 15. For a given site, the pattern of the  $FR_2^{qRMS}$  contours is similar with that of the  $FR_1^{qRMS}$  contours; however, the former contours have larger values and are characterized by the occurrence of multiple distinctive peaks distributed at: (a)  $0.25 \text{ m} < H_s < 3.25 \text{ m}$  and  $3.0 \text{ s} \leq T_p < 8.0 \text{ s}$  (site S1, Figure 13), (b)  $0.25 \text{ m} < H_s < 4.25 \text{ m}$  and  $3.0 \text{ s} \leq T_p < 9.0 \text{ s}$  (site S2, Figure 14) and (c)  $0.25 \text{ m} < H_s < 4.75 \text{ m}$  and  $3.0 \text{ s} \leq T_p < 10.0 \text{ s}$  (site S3, Figure 15).

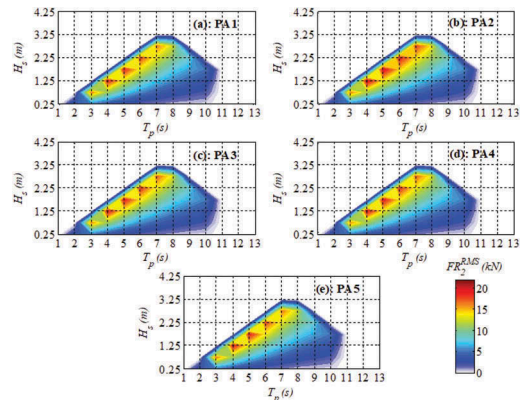


Figure 13.  $FR_2^{qRMS}$ ,  $q=1, \dots, 5$ , contours for optimally-arranged array at S1.

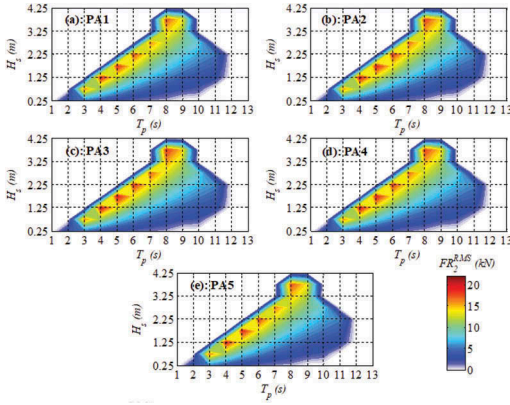


Figure 14.  $FR_2^{qRMS}$ ,  $q=1, \dots, 5$ , contours for optimally-arranged array at S2.

It is also interesting to note that irrespectively of the deployment site, the  $FR_2^{qRMS}$  global peak for each  $q$ -th PA occurs for sea states with  $H_s=1.25$  m and  $T_p=4.0$  s. The energy content of the input wave spectra for this sea state is smaller compared to the  $H_s, T_p$  combinations where the rest peak values occur (e.g.  $H_s=1.75$  m and  $T_p=5.0$  s,  $H_s=2.25$  m and  $T_p=6.0$  s). However, the decreasing trend of the  $FR_2^q$ ,  $q=1, \dots, 5$ , transfer functions towards smaller frequencies at  $\omega < 2$  rad/s (Figure 6) leads to restraining loads spectra of higher energy content for  $H_s=1.25$  m and  $T_p=4.0$  s (results are not included here due to space constraints) and, thus, to larger  $FR_2^{qRMS}$  values.

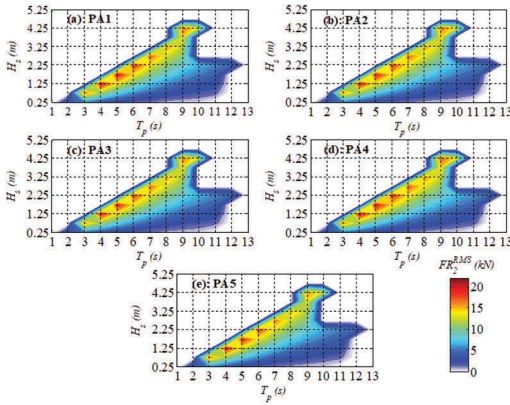


Figure 15.  $FR_2^{qRMS}$ ,  $q=1, \dots, 5$ , contours for optimally-arranged array at S3.

For a given marine site and sea state, insignificant differences are observed on the  $FR_2^{qRMS}$  values among the various PAs, in accordance with the relevant discussion previously made in the case of Figure 6. Furthermore, for sea states common at all three sites, the realization of different optimum layouts combined with the existence of different wave climate conditions at S1-S3 affect at a small degree the  $FR_2^{qRMS}$  values. Accordingly, for all PAs and for all sites examined the

$FR_2^{qRMS}$  global peaks (for  $H_s=1.25$  m and  $T_p=4.0$  s) are approximately equal to 19.6 kN.

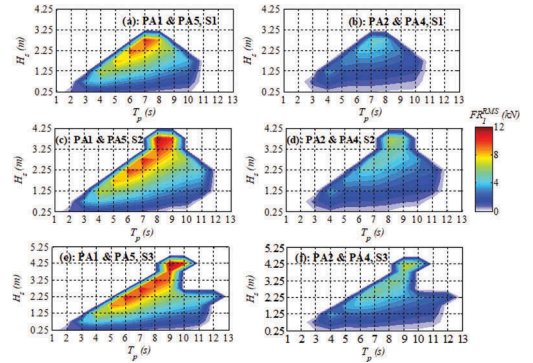


Figure 16.  $FR_1^{qRMS}$ ,  $q=1, 2, 4$  and  $5$ , contours for equally-spaced arrays at S1-S3.

Moving on to the equally-spaced arrays, the corresponding  $FR_1^{qRMS}$ ,  $q=1, 2, 4$  and  $5$ , contours are shown in Figure 16 for all sites examined. For each site and PA, the aforementioned contours have the same pattern as in the case of the optimally-arranged arrays (Figs 10-12). However, the existence of equally-spaced PAs increases the values of  $FR_1^{qRMS}$ ,  $q=1, 2, 4$  and  $5$ . For example, in the case of PA1 and PA5, where the largest surge restraining loads are applied, the global peaks of  $FR_1^{qRMS}$ ,  $q=1$  and  $5$ , are equal to 10.6 kN (site S1), 12.1 kN (site S2) and 12.1 kN (site S3). The above

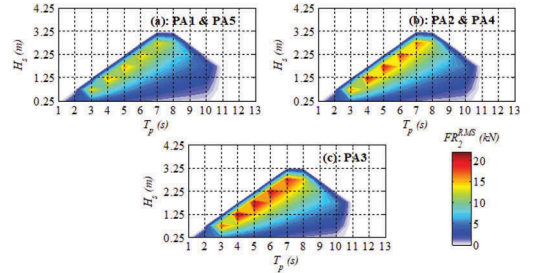


Figure 17.  $FR_2^{qRMS}$ ,  $q=1, \dots, 5$ , contours for equally-spaced arrays at S1.

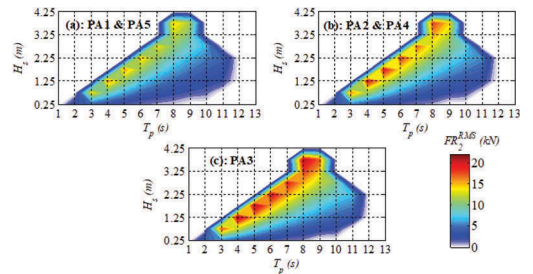


Figure 18.  $FR_2^{qRMS}$ ,  $q=1, \dots, 5$ , contours for equally-spaced arrays at S2.

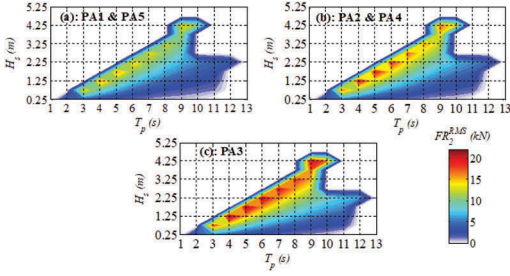


Figure 19.  $FR_2^{qRMS}$ ,  $q=1, \dots, 5$ , contours for equally-spaced arrays at S3.

correspond to an average (over all sites) increase of 34% and 42% for PA1 and PA5 respectively compared to the case of optimally-arranged arrays.

Finally, with regard to the sway restraining loads applied on the PAs of equally-spaced arrays, Figures 17, 18 and 19 show the contours of  $FR_2^{qRMS}$ ,  $q=1, \dots, 5$ , for S1, S2 and S3 respectively. Similarly to the surge restraining loads, the  $R_2^{qRMS}$  contours for a given site and PA have the same pattern as in the case of the optimally-arranged arrays (Figures 13-15). However, contrary to the latter arrays, a gradual increase of the  $FR_2^{qRMS}$  peak values is observed as we are moving from PA1 and PA5 (outer PAs) to PA2 and PA4 and, finally, to PA3 (middle PA), where  $FR_2^{qRMS}$  peaks obtain the largest values. This trend, directly related to the values of the  $FR_2^q$ ,  $q=1, \dots, 5$ , transfer functions (Figure 8), leads also to smaller or larger  $FR_2^{qRMS}$  values compared to optimally-arranged arrays, depending upon the location of the PA within the array. More specifically, considering the outer PAs, the global peaks of  $FR_2^{qRMS}$ ,  $q=1$  and 5, for the equally-spaced arrays are equal to 16.2 kN (site S1), 16.3 kN (site S2) and 16.4 kN (site S3). The corresponding values for PA2 and PA4 are 19.5 kN (site S1), 19.6 kN (site S2) and 19.9 kN (site S3), while for PA3 they are equal to 21.4 kN (site S1), 21.6 kN (site S2) and 21.9 kN (site S3). The above indicate an average (over all sites) decrease of  $\sim 18\%$  for PA1 and PA5 and of  $\sim 0.5\%$  for PA2 and PA4, as well as an average (over all sites) increase of  $\sim 10\%$  for PA3 compared to the case of optimally-arranged arrays.

## 5 CONCLUSIONS

In the present paper, we assess numerically the surge and sway restraining loads applied on the PAs of optimally-arranged linear arrays in front of a bottom-mounted vertical wall of finite length. The arrays, maximizing the yearly absorbed energy, consist of five, identical, oblate spheroidal heaving PAs and are taken to be deployed at three near-shore sites in the Aegean Sea, Greece, characterized by different local wave climates. Results are, initially, presented for regular waves and then for normal operating conditions (irregular waves), while, furthermore, they are compared with those obtained for the case of equally-spaced arrays.

Under regular waves, the surge restraining loads for all the examined optimally-arranged arrays are characterized by an intense (irregular) variation pattern, while the opposite holds true for the sway restraining loads. At  $\omega < 2$  rad/s, larger surge restraining loads are observed for the outer PAs of each array compared to the rest devices. However, the sway restraining loads have almost the same values for all the PAs, independently upon their location within the array. Moreover, for a given PA, the realization of different arrays' layouts at the three sites does not introduce any significant differences on the values of both the above loads at  $\omega < 2$  rad/s. Compared to equally-spaced arrays, the optimally-arranged ones may lead to smaller values of the surge and sway restraining loads, depending, though, on the PA and the frequency range being examined.

Under irregular waves, the contours of the RMS values of the surge and the sway restraining loads,  $FR_j^{qRMS}$ ,  $j=1, 2$ ,  $q=1, \dots, 5$ , have a different shape among the three sites as a result of the different local wave conditions (i.e. existence of different sea states at each site). For site S2 (Central Aegean) and S3 (South-Eastern Aegean) wider contours along the  $T_p$  axis are obtained, characterized by the existence of non-zero values at  $H_s \geq 3.25$  m contrary to S1 (Central Aegean). Accordingly, the observed peaks  $FR_j^{qRMS}$ ,  $j=1, 2$ ,  $q=1, \dots, 5$ , are distributed within a wider  $H_s$  and  $T_p$  range in the case of S2 and S3 compared to S1.

For a given deployment site, the largest RMS values of the surge restraining loads are obtained for the outer devices of the optimally-arranged array, while the existence of a bit more intense wave climate conditions for S2 and S3 leads also to a small increase of the  $FR_1^{qRMS}$  peak values for all the PAs compared to S1.

As for the RMS values of the sway restraining loads, the global peak of all the  $FR_2^{qRMS}$  contours, irrespectively of the deployment site, occurs for sea states with  $H_s=1.25$  m and  $T_p=4.0$  s and not for  $H_s, T_p$  combinations of a higher energy content, as a result of the variation pattern of the corresponding transfer functions. The values of the above peaks are more than double when compared with the  $FR_1^{qRMS}$  global peaks. Moreover, different local wave conditions and the realization of different optimally-arranged arrays among the three examined sites do not introduce any significant differences on the  $FR_2^{qRMS}$  global peaks for all the PAs.

Finally, compared to the equally-spaced arrays, optimum layouts leads to a reduction of the  $FR_1^{qRMS}$  values especially in the case of the outer PAs (average, over all sites, reduction equal to 34% and 42% for PA1 and PA5 respectively, contrary to a reduction of 2% and 6% for PA2 and PA4). However, the realization of optimum layouts that are not symmetrical with respect to the incident wave direction leads to the existence of surge restraining loads for PA3 contrary to the equally-spaced arrays. As for the sway restraining loads, optimally-arranged arrays affect positively these loads in the case of PA3 (average,

over all sites, reduction of the  $FR_2^{gRMS}$  global peaks by ~10% compared to equally-spaced arrays). The opposite holds true for the outer devices (average, over all sites, increase of the  $FR_2^{gRMS}$  global peaks by ~18% compared to equally-spaced arrays), while there is an insignificant effect for PA2 and PA4. Accordingly, although optimally-arranged arrays lead to an enhanced power absorption ability, positive contributions on structural integrity related issues can be identified for specific devices of the array.

The results of the present work can be further employed for either the short-term or the long-term fatigue damage analysis of the PAs components by applying appropriate relevant numerical methods. Furthermore, the present study could be extended to assess loads under extreme wave conditions for specific survival modes, by deploying numerical models that account for nonlinear effects along with the environmental contours approach. The implementation of high-fidelity numerical simulations and/or laboratory tests could also present items for future research, facilitating at the same time the validation of the present numerical approach.

## REFERENCES

- Ahamed, R., McKee, K. & Howard, I. 2020. Advancements of wave energy converters based on power take off (PTO) systems: A review. *Ocean Engineering* 204:107248.
- Bergdahl, L. 2009. Comparison of measured shallow-water wave spectra with theoretical spectra. In *Proc. 8th European Wave and Tidal Energy Conference, Uppsala*, 7-10 September 2009.
- Det Norske – Germanischer Lloyds (DNV – GL) 2017. *Environmental Conditions and Environmental Loads, Recommended Practice DNV RP-C205*. Oslo: Det Norske Veritas.
- European Commission 2019. *European Green New Deal, COM (2019) 640*. Brussels: European Union.
- Fang, H.W., Feng, Y.Z. & Li, G.P. 2018. Optimization of wave energy converter arrays by an improved differential evolution algorithm. *Energies* 11: 3522.
- Garcia-Teruel, A. & Forehand, D.I.M. 2021. A review of geometry optimisation of wave energy converters. *Renewable and Sustainable Energy Reviews* 139: 110593.
- Giassi, M. & Götteman, M. 2018. Layout design of wave energy parks by a genetic algorithm. *Ocean Engineering* 154: 252–261.
- Gkaraklova, S., Chotzoglou, P. & Loukogeorgaki, E. 2021. Frequency-based performance analysis of an array of wave energy converters around a hybrid wind-wave monopile support structure. *Journal of Marine Science and Engineering* 9(1): 2.
- Guo, B. & Ringwood, J.V. 2021. Geometric optimisation of wave energy conversion devices: A survey. *Applied Energy* 297: 117100.
- Hughes, S.A. 1984. *The TMA Shallow-water Spectrum Description and Applications, Technical Report CERC-84-7*. USA: Coastal Engineering Research Center, Department of the Army, US Army Corps of Engineers.
- Lavidas, G. & Venugopal, V. 2017. A 35 year high-resolution wave atlas for nearshore energy production and economics at the Aegean Sea. *Renewable Energy* 103: 401–417.
- Lee, C.H. & Newman, J.N. 2005. Computation of wave effects using the panel method. In S. Chakrabarti (ed.), *Numerical Models in Numerical Models in Fluid-Structure Interaction*: 211–251. Massachusetts: WIT Press.
- Lee, C.H. 1995. *WAMIT Theory Manual*. Available online: <https://www.wamit.com/Publications/tmanual.pdf> (accessed on 19 May 2022).
- Loukogeorgaki, E., Michailides, C., Lavidas, G. & Chatjigeorgiou, I.K. 2021a. Layout optimization of heaving wave energy converters linear arrays in front of a vertical wall. *Renewable Energy* 179: 189–203.
- Loukogeorgaki, E., Michailides, C., Lavidas, G. & Chatjigeorgiou, I.K. 2021b. Optimum layouts of a cluster of heaving point absorbers in front of a wall. In *Proc. 31st (2021) International Offshore and Polar Engineering Conference, ISOPE 2021, Rhodes, 20-25 June 2021(hybrid)*, 1: 736–743.
- Lyu, J., Abdelkhalik, O. & Gauchia, L. 2019. Optimization of dimensions and layout of an array of wave energy converters. *Ocean Engineering* 192: 106543.
- Magagna, D., Monfardini, R. & Uihlein A. 2016. *JRC Ocean Energy Status Report: 2016 Edition, EUR 28407 EN (JRC104799)*. Luxembourg: Publications Office of the European Union.
- Michailides, C. & Angelides, D.C. 2015. Optimization of a Flexible Floating Structure for Wave Energy Production and Protection Effectiveness. *Engineering Structures* 85: 249–263.
- Naess, A. & Moan, T. 2013. *Stochastic Dynamics of Marine Structures*. USA: Cambridge University Press.
- Neshat, M., Abbasnejad, E., Shi, Q., Alexander, B. & Wagner, M. 2019. Adaptive neuro-surrogate-based optimisation method for wave energy converters placement optimisation, In *Proc. 26th International Conference on Neural Information Processing, Sydney, 12-15 December 2019*, 353–366.
- Penalba, M., Touzón, I., Lopez-Mendia, J. & Nava, V. 2017. A numerical study on the hydrodynamic impact of device slenderness and array size in wave energy farms in realistic wave climates. *Ocean Engineering* 142: 224–232.
- Portillo, J.C.C., Collins, K.M., Gomes, P.F., Henriques, J.C. C., Gato, L.M.C., Howey, B.D., Hann, M.R., Greaves, D.M., & Falcão, A.F.O. 2020. Wave energy converter physical model design and testing: The case of floating oscillating-water-columns. *Applied Energy* 278: 115638.
- Ruiz, P.M., Nava, V., Topper, M.B.R., Minguela, P.R., Ferri, F. & Kofoed, J.P. 2017. Layout optimisation of wave energy converter arrays. *Energies* 10(9): 1262.
- Sarkar, D., Contal, E., Vayatis, N. & Dias, F. 2016. Prediction and optimization of wave energy converter arrays using a machine learning approach. *Renewable Energy* 97: 504–517.
- Sharp, C. & DuPont, B. 2018. Wave energy converter array optimization: A genetic algorithm approach and minimum separation distance study. *Ocean Engineering* 163: 148–156.
- Zhao, X.L., Ning, D.Z., Zou, Q.P., Qiao, D.S. & Cai, S.Q. 2019. Hybrid floating breakwater-WEC system: A Review. *Ocean Engineering* 186: 106126.